Automated Detection of Short-term Slow Slip Events in Southwest Japan

Yiming Ma[1*], **Fabien Montiel** [1]

[1]Department of Mathematics and Statistics, University of Otago

Key Points:

- We develop a change-point detection method for detecting automatically the start and end times of short-term SSEs in GPS data.
- Synthetic tests verified its validity and demonstrated that the new method outperforms two existing methods.
- We illustrate the effectiveness of the method in detecting short-term SSEs in Southwest Japan.

*Dunedin, New Zealand

Corresponding author: Yiming Ma, maym@maths.otago.ac.nz

Abstract

Inferring from the occurrence pattern of slow slip events (SSEs) the probability of triggering a damaging earthquake within the nearby velocity weakening portion of the plate interface is critical for hazard mitigation. Although robust methods exist to detect long-term SSEs consistently and efficiently, detecting short-term SSEs remains a challenge. In this study, we propose a novel statistical approach, called singular spectrum analysis isolate-detect (SSAID), for automatically estimating the start and end times of short-term SSEs in GPS data. The method recasts the problem of detecting SSEs as that of detecting change-points in a piecewise signal. This is achieved by obscuring the deviation from piecewise-linearity in the underlying SSE signals using added noise. We verify its effectiveness on a range of model-generated synthetic SSE data with different noise levels, and demonstrate its superior performance compared to two existing methods. We illustrate its capability in detecting short-term SSEs in observed GPS data using 36 GPS stations in southwest Japan via the co-occurrence of non-volcanic tremors, hypothesis tests and fault estimation.

Plain Language Summary

[SSEs, a type of slow earthquakes, are thought to play an important role in releasing strain in subduction zones, and affect the occurrence of large earthquakes, although their exact connection remains unclear. Detecting accurately the start and end times of SSEs is one prerequisite to illuminate their interactions with large earthquakes. However, no robust detection method has been well developed so far. SSEs are widely recorded by GPS network, part of the Global Navigation Satellite System (GNSS). Most undetected SSEs in GPS data are short-term SSEs, i.e. SSEs with short durations ranging from days to weeks, since the amplitude changes in the GPS data trend from short-term SSEs are somewhat small, close to (or even lower than) the background noise. Therefore, more urgent efforts should be devoted to developing a rapid automated method for detecting short-term SSEs in GPS data. In this study, we utilize a change-point detection method for piecewise signals to detect automatically the start and end times of short-term SSEs in GPS data. We demonstrate its effectiveness on both simulated and observed GPS data. The results show that the detection performance of our method regarding the number of estimated change-points and their locations outperform two existing methods.]

1 Introduction

Slow slip events (SSEs) are fault slips occurring at the subduction interface between tectonic plates. They are roughly categorized into short-term SSEs (in the order of days to weeks) and long-term SSEs (in the order of months to years) (Obara, 2020). They constitute a type of slow earthquakes (Hirose et al., 1999; Mitsui & Hirahara, 2006; Obara & Kato, 2016; Obara, 2020). SSEs play a vital role in releasing stress along subduction interfaces. The associated episodic stress perturbations on the seismogenic zone have been linked to the occurrence of larger natural earthquakes (Segall et al., 2006; Ito et al., 2013; Bartlow et al., 2014; Radiguet et al., 2016; Voss et al., 2018; Bletery & Nocquet, 2020). SSEs might also prevent the rupture of large earthquakes from propagating further along the subduction interface, while large earthquakes can also initiate SSEs in the nearby transition zone (Hirose et al., 2012; Yarai & Ozawa, 2013; Nishikawa et al., 2019; Wallace, 2020; Nishimura, 2021). Here the transition zone refers to the area where SSEs occur along the subduction interface. Understanding the process governing SSEs could potentially help us forecast impending earthquakes, although the underlying geophysical mechanism for forming SSEs remains elusive (Mazzotti & Adams, 2004; Jordan & Jones, 2010; Lohman & Murray, 2013; Beeler et al., 2014; Obara & Kato, 2016; Barbot, 2019; Obara, 2020).

Detecting SSEs accurately could be the key to determine the mechanism generating SSEs and illuminate their interactions with large earthquakes (Ikari et al., 2013; Saffer & Wallace, 2015; Ozawa et al., 2019; Nishimura, 2021). SSEs are generally recorded through geodetic measurements such as Global Navigation Satellite System (GNSS), tiltmeters and strainmeters. Among these, the Global Positioning System (GPS; one type of GNSS) network is the most popular way of recording ground movements with the intention of uncovering SSEs, because it is relatively inexpensive, easily accessible and sufficiently precise (Melbourne et al., 2005; Smith & Gomberg, 2009; Vergnolle et al., 2010; Jiang et al., 2012; Cavalié et al., 2013; He et al., 2017). Developing a robust method for detecting SSEs in GPS data is crucial, despite the many challenges it presents (Nishimura et al., 2013; Nishimura, 2014; Rousset et al., 2017; Takagi et al., 2019; Nishikawa et al., 2019; Haines et al., 2019; Nishimura, 2021; Okada et al., 2022). For ease of presentation, we refer to GPS data recording SSEs as SSE data thereafter.

Numerous methods have been proposed to detect the occurrence times of SSEs in GPS data (hereafter referred to as SSE detections). The first group of approaches is based on Kalman filter of state vector, which model the recorded GPS time series as the sum of coherent signals from various sources and estimation errors (Granat et al., 2013; Ji & Herring, 2013; Lohman & Murray, 2013; Walwer et al., 2016). These existing approaches include Network Inversion Filter (Segall & Matthews, 1997; Segall et al., 2000; Miyazaki et al., 2003; McGuire & Segall, 2003), Monte Carlo Mixture Kalman Filter (Fukuda et al., 2004, 2008), Network Strain Filter (Ohtani et al., 2010), and further improvements on the above Kalman-filter-based methods (Ji & Herring, 2013; Riel et al., 2014; Bedford & Bevis, 2018). All these methods assume that the underlying model can completely extract the pure SSE signal from the noisy GPS data. This assumption is under debate, however, because the underlying mechanism that governs SSEs remains unclear (Obara & Kato, 2016; Obara, 2020).

Another group of approaches consists of estimating the time evolution of the slip distribution on the fault by inverting the recorded GPS data at different sites, so that the occurrence times of SSEs can be simultaneously estimated (McCaffrey, 2009; Bartlow et al., 2014; Williams & Wallace, 2015; Wallace et al., 2017, 2018). One commonly used tool for such detection is TDEFNODE, which is a nonlinear time-dependent inversion code (McCaffrey, 2009). This tool utilizes simulated annealing to downhill simplex minimization, which has been applied to invert various recorded GPS data for detecting SSEs. Two free parameters in this method are the occurrence times and the associated amplitude of SSEs (McCaffrey, 2009). TDEFNODE needs *a priori* information on the functional form (e.g. exponential or Gaussian) of the temporal evolution of SSEs on the fault. However, the selection of a suitable form remains enigmatic, and is generally determined by trial tests (Wallace et al., 2017). In addition, the geometry of the subduction zone must be known to use TDEFNODE, thus its application is affected by the availability of geometrical knowledge in the observed data.

Singular Spectrum Analysis (SSA), a univariate time series analysis method (Ghil et al., 2002), can remedy this latter shortcoming. SSA is designed to extract information from noisy time series and thus, provides insight into the underlying dynamics (Ghil et al., 2002). The key feature of this method is that it does not need any *a priori* knowledge of the underlying pure signal, and the trends obtained in this way are not necessarily linear (Ghil et al., 2002; Chen et al., 2013). SSA typically decomposes the noisy data into reconstructed components (RCs). These RCs are sorted in a descending order according to their corresponding eigenvalues, which denote their proportions of the total variance of the original data. Low-order RCs in the queue are regarded as effective signals related to the underlying dynamics, while high-order RCs are taken as noise, and are typically discarded. This is the common way to extract pure SSEs from noisy data by SSA. To determine a threshold between pure signal RCs and noise RCs is relatively subjective. When the signal-to-noise ratio (SNR) is low, SSA normally fails to

distinguish signal from noise. Chen et al. (2013) demonstrated that SSA is a viable and complementary tool for extracting modulated oscillations from GPS time series.

Walwer et al. (2016) introduced a more powerful form of SSA, Multichannel Singular Spectrum Analysis (M-SSA), to extract SSEs. M-SSA can simultaneously make use of the spatial and temporal correlations to explore the spatiotemporal variability of the data set. Although M-SSA was shown to outperform many existing detection methods, it still has drawbacks. This method only aims at extracting SSEs without detecting the occurrence times of SSEs, so a follow-up detection to determine the start and end times of SSEs is needed. The size of the lag covariance matrix in M-SSA also grows rapidly with the size of the GPS network considered, leading to computational issues for large-scale networks. M-SSA cannot operate on a single data basis, which limits its applicability to cases where the signals lack spatial coherence, for example, when there are not enough GPS stations, or the stations are too close to each other. Relative Strength Index (RSI), a single-station technique from the stock market (Crowell et al., 2016), is able to solve all the aforementioned issues, but it only applies to long-term SSEs.

Compared to long-term SSEs, the duration and recurrence interval of short-term SSEs are much smaller, in the order of several days or weeks. The amplitude change in the GPS data caused by a short-term SSE is also relatively small. It can be close to, or even lower than, the background noise, so most short-term SSEs remain undetected (Nishimura, 2021; Yano & Kano, 2022). Therefore, more urgent efforts should be devoted to rapid automated methods for detecting short-term SSEs (Hirose & Kimura, 2020; Obara, 2020; Okada et al., 2022), which is the focus of our current study. Linear regression, combined with Akaike's Information Criterion (AIC), is widely used to detect short-term SSEs for large-scale GPS networks (Nishimura et al., 2013; Nishimura, 2014, 2021; Okada et al., 2022). This method fits linear functions with and without an offset, and then uses AIC to judge which function is a better fit considering a number of free parameters. In this method, the length of the designed sliding window and the user-defined detection threshold determine the detection accuracy. In practice, it is hard to select reasonable values for these subjective parameters (Nishimura et al., 2013; Yano & Kano, 2022; Ma et al., 2022). A new method developed by Yano and Kano (2022) can overcome this deficiency, approximating SSE data as piecewise-linear signals by using l_1 trend filtering combined with Mallows' C_p. The knots in the fitted piecewise-linear signal are then taken as the occurrence times of SSEs. The applications to both synthetic and observed SSE data demonstrated that this method obtained better performance than the linear regression method. However, it is not clear that the assumption that SSE data can be regarded as piecewise-linear signals with the knots being the occurrence times of SSEs is reasonable, since the specific form of the underlying SSE signal remains unknown (Obara & Kato, 2016; Obara, 2020).

In this study, we develop a new method, called Singular Spectrum Analysis Isolate-Detect (SSAID), to automatically detect the start and end times of short-term SSEs in GPS data. This method regards the detection of short-term SSEs in GPS data as a problem of detecting change-points in piecewise non-linear signals, in which the start and end times of SSEs are change-points to be detected. The prominent advantage of SSAID is that it does not require prior knowledge of the exact form of the underlying SSE signal. SSAID aims to obscure the differences between the nonlinear SSE signal and a piecewise-linear model, so that existing change-point detection methods for piecewise-linear signals can be directly applied to detect the start and end times of short-term SSEs. This is done by (i) decomposing the noisy SSE data into spectral components through SSA (Ghil et al., 2002) and reconstructing these components into new noisy data signals; (ii) adding noise to these reconstructed signals, and (iii) conducting the detection by Isolate-Detect (ID; Anastasiou & Fryzlewicz, 2021). We conduct a range of simulations to evaluate the detection performance of SSAID using both simulated and observed SSE data.

In Section 2, we introduce the observed SSE data in southwest Japan and the associated data processing procedures. In Section 3, we introduce the method SSAID along with some assumptions. In Section 4, we show results of applying SSAID to a range of simulated SSE data and compare the results with two existing detection methods (i.e. linear regression with AIC; and l_1 trend filtering). In Section 5, we demonstrate its capability in detecting short-term SSEs in observed GPS data. Discussions and conclusions are in Section 6.

2 Data and processing

We use SSE data from the Nankai subduction zone which has a dense geodetic observation network. In southwestern Japan, the Amurian plate overriding the Philippine Sea plate converges to N50°W at a rate of about 67 mm/year (Miyazaki & Heki, 2001; Nishimura, 2014; Kano & Kato, 2020; Obara, 2020). Both long-term and short-term SSEs occur across the Nankai Trough (Obara, 2020) (see Fig. 1 (a)). Short-term SSEs in southwest Japan generally exist in the deeper extension of long-term SSEs regions.

We use SSE data from 36 GPS stations of the GNSS Earth Observation Network System (GEONET) operated by the Geospatial Information Authority of Japan (GSI). These GPS stations are distributed in the Shikoku region along the Bungo Channel (see Fig. 1 (b)). The analysis period for this study is from 1 January 2008 to 30 June 2009. The vector of coordinates at each GPS station, containing east, north and upward displacement, has been transformed to the 2005 International Terrestrial Reference Frame (ITRF2005), and can be generally modelled as a sum of different processes (Nikolaidis, 2002; Davis et al., 2012; He et al., 2017; Bedford & Bevis, 2018), that is

$$\mathbf{u}(t) = \mathbf{d_0} + \mathbf{m_0}t + \sum_{j=1}^{n_o} \mathbf{b_j} H(t - t_j) + \sum_{i=1}^{n_s} \mathbf{h_i}(t - t_i) + \boldsymbol{\xi_1}(t) + \boldsymbol{\xi_2}(t) + \boldsymbol{\xi_3}(t) + \boldsymbol{\epsilon}(t), \qquad (1)$$

where t is the time, $\mathbf{d_0}$ and $\mathbf{m_0}$ refer to vectors describing the position of the reference site and the secular velocity, respectively. Here, we refer to the displacement rate of the linear process without the occurrence of other fault slips as the secular velocity, which represents the secular tectonic motions of two contacting plates of the subduction zone. The third term $\sum_{j=1}^{n_o} \mathbf{b_j} H(t-t_j)$ describes the vector of offsets due to non-tectonic changes such as antenna or other instrument changes, where n_0 is the number of non-tectonic changes, t_j is the time when the j-th non-tectonic change occurs, and $H(t)$ is the Heaviside step function. The fourth term $\sum_{i=1}^{n_s} \mathbf{h_i}(t-t_i)$ represents the vector of coseismic and postseismic movements from ambient regular earthquakes, where n_s is the number of ambient regular earthquakes, t_i is the time at which the i-th regular earthquake occurs, and $\mathbf{h_i}$ refers to the coseismic and postseismic movements from the i-th regular earthquake (Wdowinski et al., 1997; ElGharbawi & Tamura, 2015). The other vectors $\boldsymbol{\xi_1}(t)$, $\boldsymbol{\xi_2}(t)$, $\boldsymbol{\xi_3}(t)$ and $\boldsymbol{\epsilon}(t)$ describe the movements from seasonal motions, unknown sources, SSEs and noise, respectively.

These SSE data have been pre-processed by Nishimura et al. (2013) to remove known effects from non-SSE processes. We now briefly illustrate the data processing procedures conducted on the raw GPS data (Nishimura et al., 2013; Nishimura, 2014; Fujita et al., 2019; Nishimura, 2021). Firstly, they eliminated the coseismic offsets from six ambient large earthquakes (see the detailed catalogue therein), which are estimated by the difference in the 10-day averages of the daily coordinates before and after the earthquakes. Secondly, the spatial filtering technique of Wdowinski et al. (1997) was applied to suppress the common mode errors for these stations, which are a major type of spatially correlated noise sources in GPS data (Dong et al., 2006). Finally, the offsets from non-tectonic changes (i.e. the third term in Eq. (1)) such as antenna maintenance were removed by the same method as that used to remove coseismic offsets. Note that the post-seismic deformations from nearby large earthquakes were not removed (i.e. the fourth term in

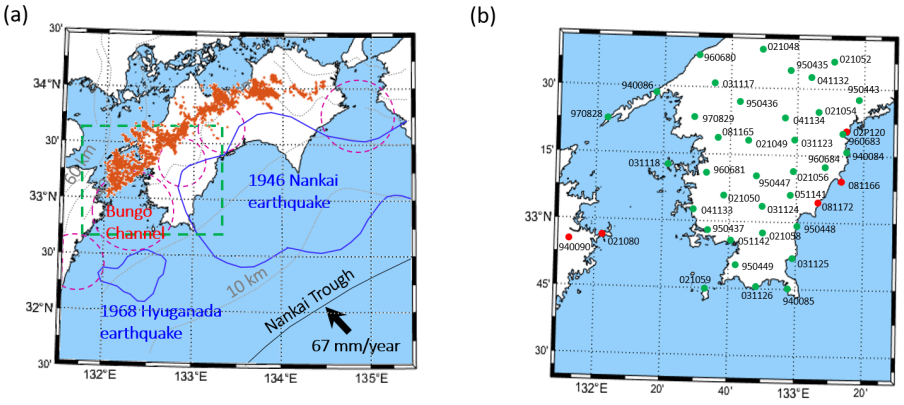

Figure 1. (a) The distribution map of earthquakes in the study area of southwest Japan. The magenta dashed circles and the blue contours denote the source areas of long-term SSEs and megathrust earthquakes, respectively. The orange dots show the epicenters of tremors. Gray dashed lines indicate the depth of the subducting Philippine Sea plate. (b) The distribution map of 36 GPS stations utilized in the current case study (see Section 5). This area is outlined by the dashed green box in panel (a). Both red and green circles indicate the location of GPS stations, and the numbers near to circles refer to the GPS station names. Note that we apply SSAID to detect change-points in SSE data recorded by GPS stations identified as green filled circles in the case study reported in Section 5.

Eq. (1)), however their impacts are negligible in our current application as no obvious large earthquakes were identified in the period analyzed (i.e. from January 1 2008 to June 30 2009) in the research area (Nishimura et al., 2013).

We denote the processed daily cumulative displacement vector at each station as

$$\bar{\mathbf{u}}(t) = \bar{\mathbf{b}}_{\mathbf{0}} t + \bar{\boldsymbol{\xi}}_{\mathbf{1}}(t) + \bar{\boldsymbol{\xi}}_{\mathbf{2}}(t) + \bar{\boldsymbol{\xi}}_{\mathbf{3}}(t) + \bar{\boldsymbol{\epsilon}}(t), \tag{2}$$

where $\bar{\mathbf{b}}_{\mathbf{0}}$ is the vector of coefficients quantifying the secular movement, and $\bar{\boldsymbol{\xi}}_{\mathbf{1}}(t)$, $\bar{\boldsymbol{\xi}}_{\mathbf{2}}(t)$, $\bar{\boldsymbol{\xi}}_{\mathbf{3}}(t)$ and $\boldsymbol{\epsilon}(t)$ are vectors of daily cumulative displacements of seasonal motions, unknown sources, SSEs and noises, respectively. The daily cumulative displacement $\bar{\mathbf{u}}(t)$ contains three components along different directions (i.e. east, north and upward), which are denoted as $\bar{u}_e$, $\bar{u}_n$, $\bar{u}_z$, respectively. In the following application, we concentrate on the N50°W component of the daily cumulative displacement at each station, denoted by X_t, which is parallel to the plate convergence direction of the Nankai Trough (see Fig. 1 (a)). This is done by rotating two horizontal components (i.e. east and north) using the following equation,

$$X_t = \bar{u}_e \sin\bar{\delta}_0 - \bar{u}_n \cos\bar{\delta}_0, \tag{3}$$

where $\bar{\delta}_0$ is the azimuth angle of the plate convergence direction (see the black arrow in Fig. 1 (a); $\bar{\delta}_0 \approx 50°$ in Nankai Trough). In the following applications, we further remove the daily secular motions and outliers from X_t at each station, through linear least squares and the four-sigma limit, respectively (Nishimura, 2021). Note that when conducting hypothesis tests in Section 5.1.2, we do not remove the daily secular motions, as they can be used to investigate the sign change of the displacement rate from the secular velocity when SSEs arise (Yano & Kano, 2022).

3 Method

We developed a new method to detect change-points in uni-variate time series with piecewise continuous structure. Here, change-points refer to the times at which the pattern of the underlying dynamics (i.e. pure signal) changes from one state to a different one. Fig. 2 (a) shows an example of observed SSE data from the Hikurangi subduction zone, New Zealand. In periods no SSEs occur, the overall trend of the signal is linear and decreasing. The trend is then redirected to a different state (increasing here) when an SSE starts. Once the SSE ends, the trend reverses back to its original linear decreasing state. The start and end times of SSEs can therefore be regarded as change-points in GPS data. Our method, called Singular Spectrum Analysis Isolate Detect (SSAID), seeks to detect the start and end times of SSEs in noisy GPS data without prior knowledge of the underlying structure of the signal. A full exposition of SSAID, including applications to data from various disciplines, can be found in Ma (2022) and Ma et al. (2022). Here, we only summarize its underlying assumptions and main features.

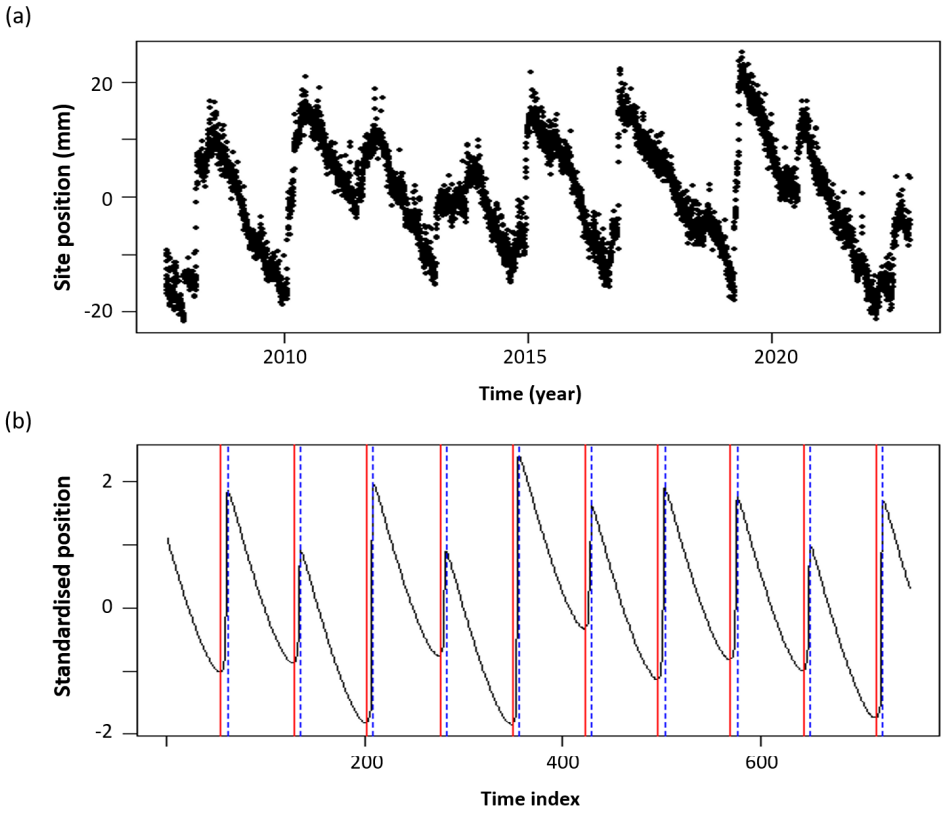

Figure 2. (a) Observed SSE data recorded by the east component of a GPS station (MAHI), in the Hikurangi subduction zone, New Zealand; (b) Synthetic SSE data with 10 SSEs in a two-year period, which are simulated by a deterministic subduction slip model (see the supplement). Red vertical lines: the start times of SSEs; blue dotted vertical lines: the end times of SSEs.

Let us assume that the deviation of the pure SSE signal from a piecewise-linear function can be obscured by noise as long as the noise level is within a suitable range. If satisfied, an existing change-point detection method for piecewise-linear signals can be directly applied to detect change-points in SSE data (Ma, 2022). This assumption was val-

idated using numerical tests in Ma (2022), in which various change-point detection methods for piecewise-linear signals were shown to successfully detect change points after different levels of Gaussian noise were added to the signal. Of all the methods considered, Isolate-Detect (ID; Anastasiou & Fryzlewicz, 2021) showed the best performance and was therefore selected for application to SSE data. The noise level within a suitable range, i.e. allowing successful change-point detection, is referred to as a suitable noise level (SNL). We further define a successful detection when two conditions are met: (1) the number of estimated change-points is exactly the number of true change-points and (2) the root mean squared error (RMSE) of the detected change-point times is less than a predefined threshold value, here 3 days.

As the SNL varies with signal types (Ma et al., 2022), it is not possible to predetermine if the raw data has an SNL. By decomposing the raw data and systematically adding Gaussian noise, SSAID generates new time series with SNL (referred to as in-SNL data), greatly improving the probability of successful change-point detection.

SSAID contains four main steps: (1) decomposing and reconstructing the signal using SSA; (2) adding Gaussian noise with different noise levels to reconstructed signals; (3) detecting change-point candidates in SSE data via ID and identifying in-SNL data and (4) determining the final change-points to best characterize the start and end times of SSEs. Brief descriptions for each step are provided as follows. The reader is referred to Ma (2022) and Ma et al. (2022) for a full exposition of the method.

1. **Signal decomposition and reconstruction:** We use SSA to decompose the input data X_t into M components by SSA, and then reconstruct M new data sequences as follows, $Y_t^k = \sum_{j=1}^{k} R_t^j$ $(k = 1, \cdots, M; t = 1, \cdots, T)$, where T is the length of the input data, and the SSA components R_t^j $(j = 1, \cdots, M)$ are sorted in decreasing order according to their correlation with the underlying dynamics. That is, R_t^j with small j values are important components of the underlying signal, while those with large j values mostly contain noise. Therefore, the noise level in Y_t^k increases with k.
2. **Generation of in-SNL data:** We add Gaussian noise with different noise levels into the reconstructed data Y_t^k $(k = 1, \cdots, M)$, that is $Z_t^{k,s,m} = Y_t^k + a_s \omega_t^m$ $(k = 1, \cdots, M; s = 1, \cdots, L; m = 1, \cdots, Q; t = 1, \cdots, T)$, where ω_t^m are independent, random variables sampled from the standard normal distribution $\mathcal{N}(0, 1)$; a_s is the level of added noise; L and Q are the number of realisations and the number of noise levels considered, respectively. The aim of this step is to guarantee the existence of in-SNL data among these newly created $Z_t^{k,s,m}$ time series. For each reconstructed signal k and noise level s, we refer to the set of all realisations $\boldsymbol{G}^{k,s} = \{Z_t^{k,s,1}, \cdots, Z_t^{k,s,Q}\}$ as a group. A group is then called an in-SNL group if the noise level of its members is an SNL.
3. **Identification of in-SNL data:** This step consists of identifying in-SNL data group-by-group among the above $Z_t^{k,s,m}$ by (1) applying ID to estimate the number of change-points $\hat{N}^{k,s,m}$ and the location of the change-points in each $Z_t^{k,s,m}$; (2) calculating three statistical quantities for each group and imposing conditions to identify in-SNL groups and then (3) taking all the members in the same group as in-SNL data.
4. **Estimation of change-points:** We determine the location of the estimated change-points in the raw data X_t using the estimated change-points for all the identified in-SNL data through a majority voting rule. This is done by (1) calculating the mode of the number of estimated change-points for each in-SNL group; (2) taking the mode of the distribution of calculated modes as the number of estimated change-points in the raw data $\hat{N}_X$; (3) collecting the estimated change-points of all the in-SNL data which have the same number of estimated change-points as $\hat{N}_X$ into the same matrix D; and then (4) taking the mode of each column in D as the location of an estimated change point in the raw data X_t.

4 Tests on synthetic data

We now evaluate the detection performance of our method for a range of simulated noisy SSE data X_t, which are generated in the following form,

$$X_t = f_t + C_{wn} \times \epsilon_t, \quad (t = 1, \cdots, T), \tag{4}$$

where T is the length of the noisy data, and f_t is the simulated pure SSE data (see Fig. 2 (b)) from a deterministic subduction slip model (see details in the supplement), which is standardised through the Z-score normalisation. The number of true change-points in the simulated pure SSE signal is $N_0 = 20$. The second term $C_{wn} \times \epsilon_t$ in Eq. (4) denotes the noise model contained in X_t. We assume that ϵ_t are independent, Gaussian random variables with mean zero and variance one. The noise level C_{wn} is the standard deviation of the noise model, varing from 1 to 100%, with increments of 1%. Fig. 3 (c) and (d) show two examples of simulated noisy SSE data with different noise levels. Using different seeds, we create 100 data sequences of independent standard Gaussian random variables ϵ_t $(t = 1, 2, \ldots, T)$. In total, we have 100×100 noisy time series X_t $(t = 1, 2, \ldots, T)$. The detection performance of SSAID is controlled by three parameters: the number of SSA components M, the number of realisations Q, and the highest level of added noise levels in percentage L. Based on numerical studies (Ma et al., 2022), we choose the default values $M = 100$, $L = 80$ and $Q = 40$ to ensure optimal performance.

4.1 Detection results

Fig. 3 (a) shows the error between the number of estimated change-points $\hat{N}_X$ by SSAID and the number of true change-points N_0 for each noisy time series. We can observe that SSAID correctly estimates the number of true change-points in over 70% of all cases analyzed. In particular, the number of estimated change-points is correct for all the cases with noise levels lower than 25% (see green box in Fig. 3 (a)). To quantify the detection performance of SSAID, we define

$$R_{sd} = \frac{\alpha}{\xi} \quad \text{and} \quad R_1 = \frac{\beta}{\xi}, \tag{5}$$

where ξ is the number of simulations for each noise level (i.e. $\xi = 100$ here), α is the number of successful detections (see the definition of a successful detection in Section 3), and β is the number of detections for which the number of estimated change-points, $\hat{N}_X$, is equal to the number of true change-points N_0 (i.e. $\hat{N}_X = N_0 = 20$ here), but not with the RMSE requirements imposed on α.

Fig. 3 (b) shows that R_{sd} and R_1 are different. They are both 100% when $C_{wn} <$ 25%, and then decrease with increasing C_{wn} values. This implies that the success detection rate is higher when the GPS data has a smaller noise level, with 100% success rate if the noise level is less than 25%. R_{sd} decreases faster than R_1 when C_{wn} increases, indicating that the accuracy of the detected change-point locations fades with increasing C_{wn} values. Fig. 3 (c) demonstrates the high accuracy of the change-points detected using our method for data with a low noise level. Fig. 3 (d) shows that when the noise level is very high ($C_{wn} = 100\%$), the locations of some detected change-points are not as accurate. The effect of the noise level C_{wn} on the performance of our method comes from a deficiency in SSA, which generally fails to distinguish the underlying signal from the noise itself when the SNR in the raw data is too low.

4.2 Comparison with two existing methods

We now compare the detection performance of SSAID with two existing detection methods for short-term SSEs. The first one is linear regression combined with AIC proposed by Nishimura et al. (2013), which has been widely applied in different areas (Nishimura et al., 2013; Nishimura, 2014, 2021; Okada et al., 2022). This method (1) uses a sliding

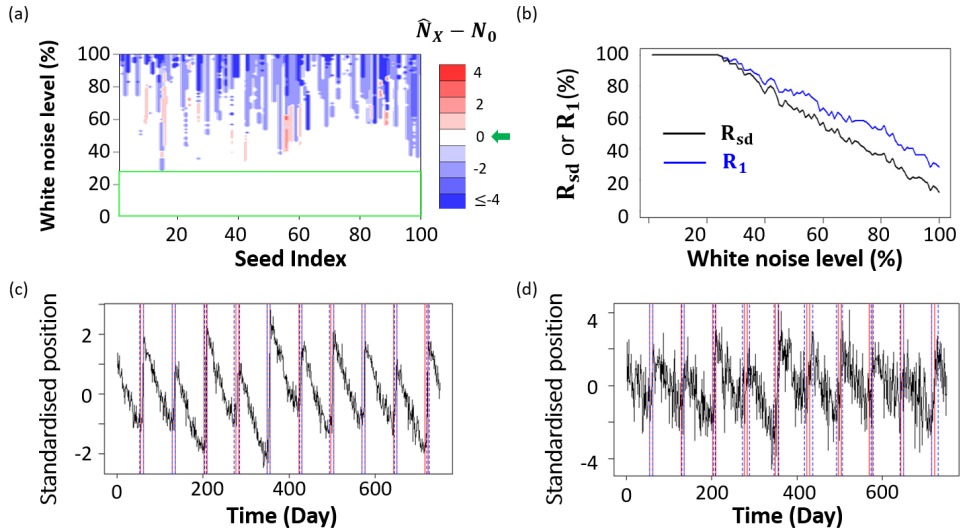

Figure 3. (a) The error between the number of estimated change-points $\hat{N}_X$ by SSAID and the number of true change-points N_0 in each simulated noisy data. The error of zero is highlighted by a green arrow in the color bar. (b) The percentage R_1 and R_{sd} (see definitions in Eq. (5)) as a function of white noise level C_{wn}, calculated from 100 seeds. The locations of the change-points in two simulation examples with different noise levels are shown in (c) $C_{wn} = 25\%$; (d) $C_{wn} = 100\%$. Blue vertical dotted lines: estimated change-points by SSAID; red vertical lines: true change-points.

window with a fixed width; (2) fits a linear model to the data in the window; (3) divides the data in the window into equal halves and fits a linear model to each half, and (4) calculates the AIC difference (i.e. ΔAIC) between the single linear model and the two-line model at the middle point of the window. If that midpoint is a change-point, e.g. the start- or end-point of an SSE, the two-line model fits the observational data better than a single linear model, thus resulting in a negative ΔAIC. As a negative ΔAIC does not always correspond to change-points in SSE signals, we must specify an appropriate threshold, denoted by ζ, in order to detect change-points of SSEs. If ΔAIC is lower than ζ, its corresponding time is regarded as a change-point. The detection performance of the linear regression approach is mainly controlled by the length of the sliding window and the specified threshold ζ, however, and selecting appropriate values for the two parameters is subjective (Nishimura et al., 2013; Nishimura, 2021).

In our comparison tests, we first take a sliding time window of 180 days, which is consistent with that of Nishimura et al. (2013), to calculate ΔAIC for each data point of the simulated SSE data in Fig. 3 (c) and (d). Fig. 4 (a) and (b) show ΔAIC values across the time series with three threshold values for ζ (high, medium and low). We observe that the change-points at both ends of the simulated data are blinded regardless of the selected thresholds due to the excessive length of the sliding window. This demonstrates that a smaller sliding window is needed (Yano & Kano, 2022). We then decrease the sliding window to 15 days to calculate ΔAIC for each data point again, and we have a much shorter blinded interval of 7 days at both ends of the simulated period. In Fig. 4 (c) and (d), we also observe that none of the detection thresholds considered succeeds in finding all the true change-points accurately. When ζ is too low, only the most significant SSEs can be detected, while for larger ζ, the detection generally overestimates the number of change-points. The selection of the threshold value depends on the signal itself, making it impossible to detect all the change-points in multiple time series or even within a single time series by using a single threshold.

We then apply the method proposed by Yano and Kano (2022) to the synthetic data (see Fig. 3). The method (1) applies l_1 trend filtering to the raw data with a range of hyperparameters λ; (2) obtains a fitted piecewise-linear signal for each λ; (3) calculates the associated Mallows' C_p for each λ; (4) chooses the one with the minimum Mallows' C_p as the best piecewise-linear approximation to characterize the raw data; and (5) takes the knots of the chosen piecewise-linear model as the occurrence times of SSEs. This method is similar to other change-point detection methods for piecewise-linear signals, for which Ma et al. (2022) have demonstrated that they cannot be directly applied to detect SSEs in GPS data. Fig. 5 (a) and (b) show that in most cases l_1 trend filtering overestimates the number of change-points in simulated SSE data and its associated successful ratio R_{sd} for each noise level is much lower than that of SSAID, regardless of the noise level.

We now compare the performance of the aforementioned methods quantitatively by calculating the total number of detected change-points across all considered scenarios (i.e. all noise levels and all seeds), as well as the counts of correct and false detections. A change-point is considered correct if its error is no more than 3 days from any true change-point location; otherwise, it is regarded as false. Both the total number of detected change-points and the number of correctly detected change-points are expected to be $20 \times 10,000$. In Fig. 6 (a), we can see that the method SSAID aligns well with the expected values, exhibiting a satisfactory total number of detected change-points and a considerable number of correct detections, with minimal false detections. However, when using the l_1 trend filtering method, we observe that the total number of detected change-points is about twice the expected value, indicating an equal number of false and correct detections. The results obtained with the method of linear regression with ΔAIC underscore the significant influence of the chosen threshold on the success of detection. Setting the threshold to a low value results in a large number of false detections. Conversely, raising the threshold ζ to a medium value (see -20 in Fig. 6 (a)) can significantly

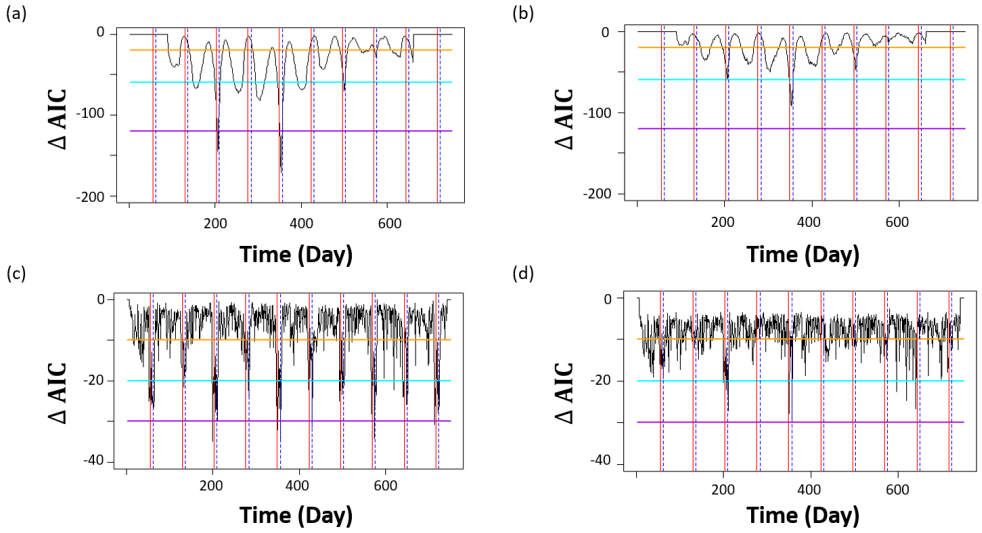

Figure 4. The calculated ΔAIC for different noisy data with different sliding windows. Panel (a) and (b) are plotted for the noisy data shown in Fig. 3 (c) and (d) with a sliding window of 180 days, respectively. While panel (c) and (d) are the same as (a) and (b) but with a sliding window of 15 days. Horizontal solid and dotted lines are associated with different thresholds to identify change-points of SSEs: high threshold (orange); medium threshold (cyan); low threshold (purple). The intersections between horizontal lines and ΔAIC curve are considered as change-points. Vertical red lines: start times of SSEs; vertical blue dashed lines: end times of SSEs.

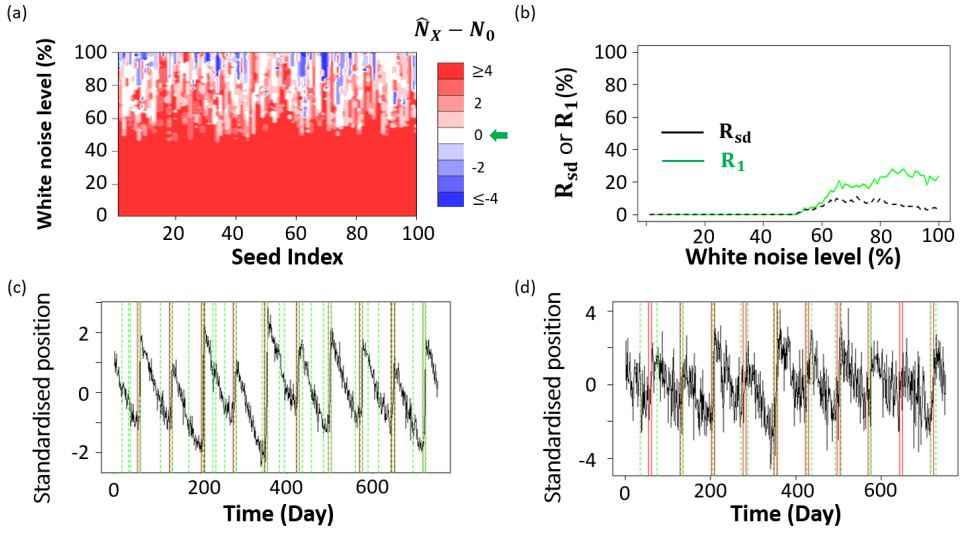

Figure 5. Same as Fig. 3 but using l_1 trend filtering to detect change-points in simulated SSE data.

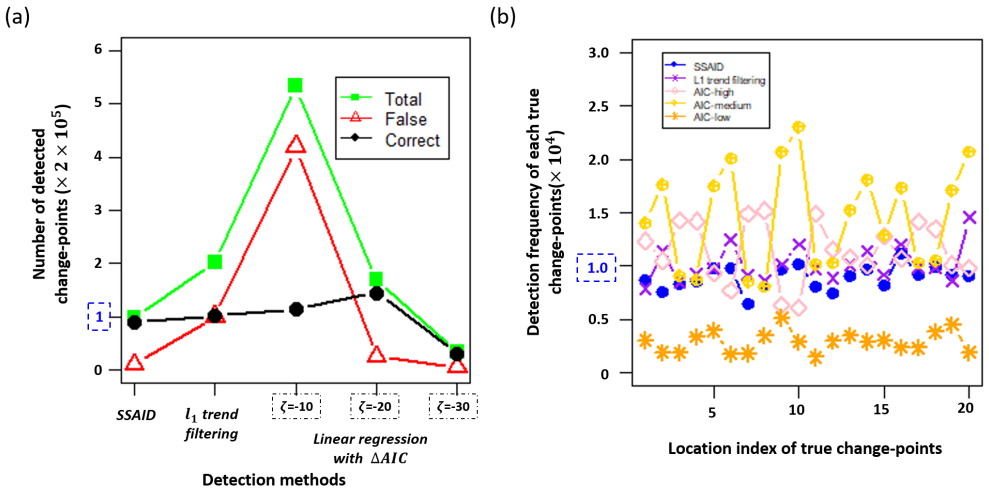

Figure 6. (a) Number of different detected change-points by various methods; (b) detection frequency of each true change-points by different methods. The expected values for the numbers of both the total and correct detected change-points are $20 \times 10,000$, while the expected value for the expected detection frequency of each true change-point is $10,000$. These expected values are highlighted by the blue dotted boxes.

reduce false detections, but leads to a notable overestimation of true change-points. Further increasing the threshold to a higher value causes the majority of detections to miss the true change-points.

We also analyze the count of successful detections for each true change-point in the simulated data. The expected detection frequency for each true change-point is $10,000$. Fig. 6 (b) shows that the detection results obtained by SSAID exhibit slight oscillations around the expected values, indicating greater stability compared to the other methods. We conduct further analysis on the histograms of the detected change-points for all the simulated noisy SSE data from all the different seeds and noise levels by these detection methods (see Fig. *S*2-*S*3 in the supplement). The results indicate that most SSAID detections tend to converge to accurate locations with minimal errors, while the other methods, despite exhibiting similar behaviors, either suffer from a higher number of false detections and larger errors, or miss the majority of true change-points. This further demonstrates the superior detection performance of SSAID.

5 Application to Observed Data

5.1 SSE detection via hypothesis testing

We first present the raw results of detected change-points in the SSE data introduced in Section 2. The change-points at each station, shown in Fig. 7 (a) (see green triangles), do not seem to exhibit a consistent pattern at first sight. In contrast to simulated SSE data (see Section 4), we do not know *a priori* when an SSE starts and ends to validate the detection. However, we can quantify the confidence that a detected change-point corresponds to an SSE by using a hypothesis test, based on the sign change of the displacement rate at the start times of SSEs from the secular displacement rate (Yano & Kano, 2022). To apply the hypothesis test, we need to know the start and end times of a potential SSE, indicating a pair of change-points are needed to define an SSE. There-

after, we refer to change-points associated with the start and end times of potential SSEs as starting and ending change-points, respectively.

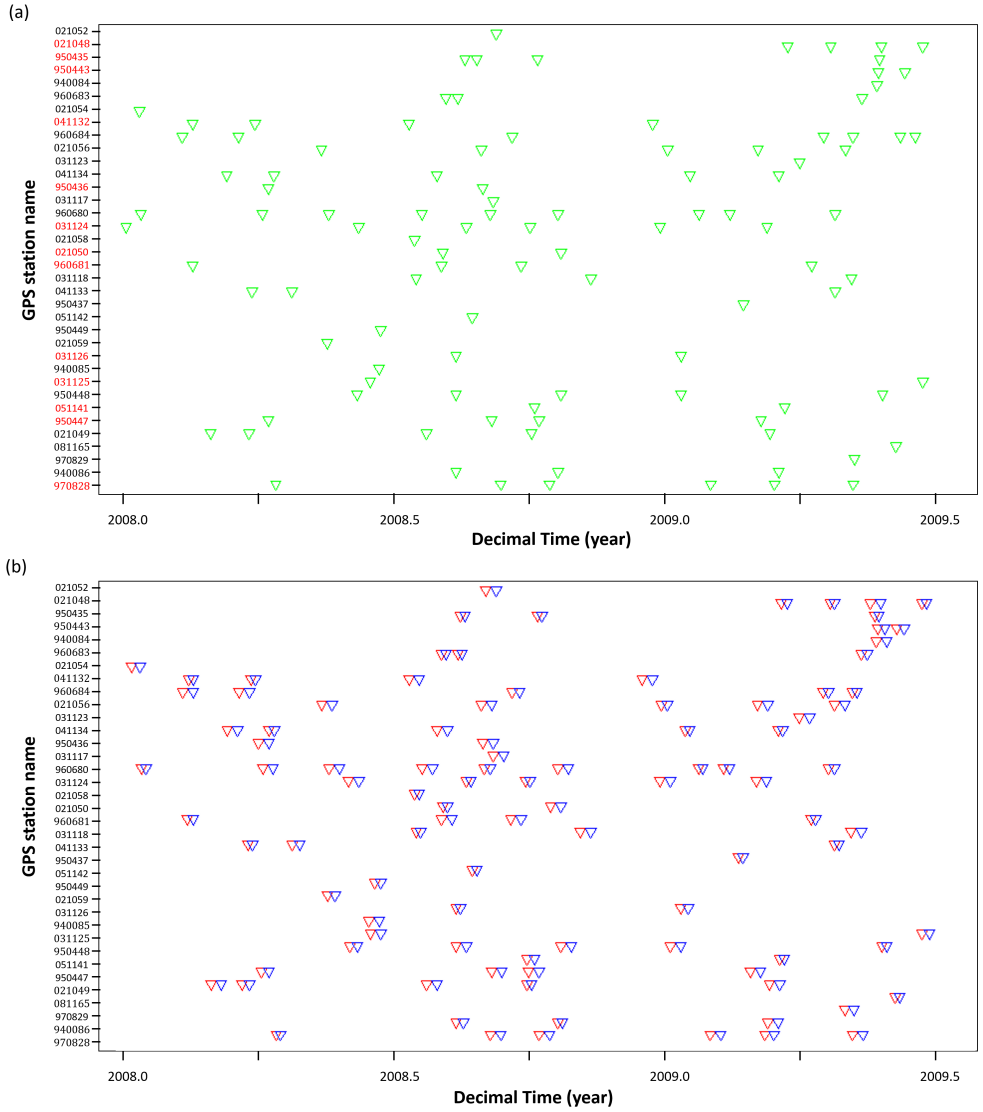

Figure 7. (a) Detected change-points by SSAID in GPS data recorded by the 36 GPS stations, shown in Fig. 1 (b). Station names for which the number of detected change-points is even are highlighted in red. (b) Pre-processed results of detected change-points shown in panel (a). Red triangles: starting change-points; blue triangles: ending change-points.

5.1.1 Pre-processing

We first pre-process the detected change-points to associate them with the start and end times of an SSE. We refer to $\hat{N}_j$ as the number of detected change-points by SSAID at the j-th station, where j is the station index ($j = 1, \cdots, 36$), which sequentially coincides with the station names on the y-axis of Fig. 7 (a) from the bottom to the top. Although we could expect all $\hat{N}_j$ to be even numbers, only 13 of them in Fig. 7 (a) are

even (see station names highlighted in red). This implies that SSAID in most stations misses some change-points associated with SSEs and/or detects spurious change-points not associated with SSEs. We also observe in multiple stations that the time difference between two neighbouring detected change-points can be in the order of months (e.g. the first and the second change-points in Fig. 8 (a), which shows the GPS data recorded at station 970828). Such a long duration is not consistent with past studies in this region, which show that potential short-term SSEs during the period analyzed last about 7 days (Hirose & Obara, 2010; Obara & Kato, 2016; Obara, 2020). Therefore, two neighbouring change-points with a large time difference cannot be paired as the start and end times of the same SSE. The above observations indicate that many single change-points were identified as potential SSEs (e.g., see green lines in Fig. 8 (a)).

To remedy this pathology, we create a change-point pair for each single change-point. The procedure contains the following five steps with details provided in the next few paragraphs: (1) we fit a piecewise-linear signal to the noisy SSE data (e.g. the orange line in Fig. 8 (a)) using the detected change-points by SSAID shown in Fig. 7 (a); (2) we calculate the slopes of each segment in the fitted model; (3) based on these slopes, we identify change-point pairs and single change-points; (4) we create several change-point pair candidates for each single change-point; and (5) we select the best candidate for each single change-point using the Schwarz Information Criterion (SIC) (Yao, 1988; Anastasiou & Fryzlewicz, 2021).

We now illustrate how to pair detected change-points based on the calculated slopes of the segments between change-points. We refer to k_b^i and k_a^i as the slope of the segment before and after the i-th detected change-point, respectively. We pair two consecutive change-points (i-th and (i+1)-th, say) as the start and end times of a unique SSE, if they simultaneously satisfy the following conditions: (1) k_b^i has the same sign as the secular displacement rate; (2) the sign of k_a^i is opposite to that of the secular displacement rate; (3) the time difference between the two neighbouring change-points (i.e. the duration of the SSE) is no more than a duration threshold, denoted by D_{max}. Here, we estimate the sign of the secular displacement rate (i.e positive or negative) at each GPS station by taking the slope of a linear model fitted to the whole noisy data. All other change-points are taken as single change-points. In the study area considered, the expected duration of an SSE is 3−7 days (Obara, 2020). Ma (2022) showed that the detected change-point location error by SSAID is at most 3 days. In the worst case, an SSE with duration 7 days could be detected by a pair of change-points separated by up to 14 days (assuming maximum error). Therefore, we set D_{max} as 14 days.

We then generate candidates of undetected change-points to pair with each single change-point. We first assume that each single change-point is associated with either the start or the end time of an SSE, and the duration of SSEs is $3-7$ days. This implies that the undetected change-point candidates are located in a window spanning $\pm(3-7)$ days around the detected single change-point. To be more specific, if the detected single change-point is the start time of an SSE, denoted by $\bar{x}_{\text{cp}}$, the associated change-point candidates for the undetected end time of this SSE include $\bar{x}_{\text{cp}}+3$, $\bar{x}_{\text{cp}}+4$, $\cdots$, $\bar{x}_{\text{cp}}+7$; conversely, if it is the end time of an SSE, the candidates for the start time are $\bar{x}_{\text{cp}}-7$, $\bar{x}_{\text{cp}}-6$, $\cdots$, $\bar{x}_{\text{cp}}-3$. Based on the slopes of two consecutive segments fitted in Step 2, we can determine if each single change-point is the start or the end time of an SSE. We have three possible situations: (1) if k_b^i and k_a^i have the same and the opposite sign as the secular displacement rate, respectively, then we regard the detected single change-point as the start time of an SSE; (2) if k_b^i and k_a^i have the opposite and the same sign as the secular displacement rate, respectively, then we regard the detected single change-point as the end time of an SSE; (3) in other cases, the detected single change-point can be the start time or the end time of an SSE.

Next, we fit different piecewise-linear curves through the GPS data for every combinations of change-point pair candidates. We select the piecewise-linear curve best fit-

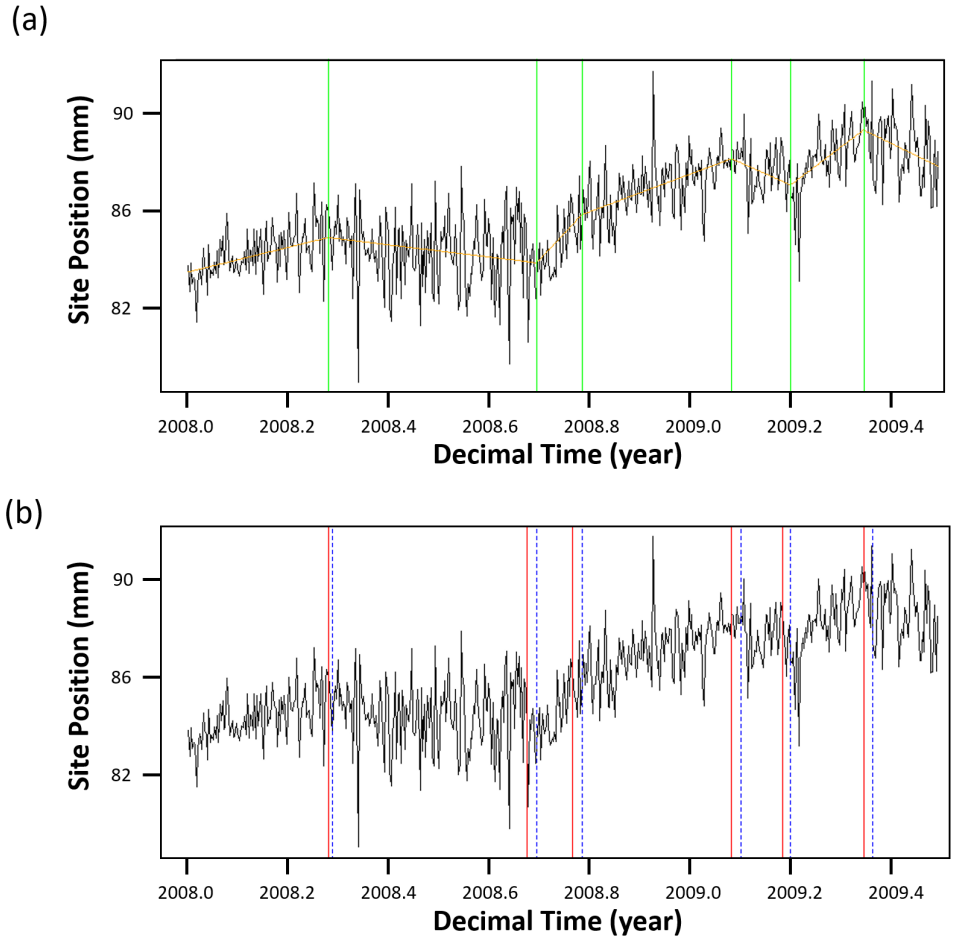

Figure 8. (a) Observed GPS data recorded by station 970828 (see the black line) and the fitted piecewise-linear signal (see the orange line) using detected change-points by SSAID (see green lines); (b) New paired change-points of the same station 970828 based on detected change-points in panel (a). Red lines: starting change-points; blue dotted lines: ending change-points.

ted to the noisy data through SIC, as suggested by numerical studies of Anastasiou and Fryzlewicz (2021), which show that the SIC-based approach exhibits better performance for piecewise signals with an intermediate number of change-points, compared to other information criteria. We then take the associated change-point candidate to pair with the single change-point, and obtain new paired change-points as shown in Fig. 7 (b) and Fig. 8 (b), in which we have two change-points for the start and end times of each potential SSE (red and blue, respectively). We denote by $\bar{N}^j = 2\bar{N}_s^j$ the number of change points at each station j after pairing the single change-points, where $\bar{N}_s^j$ is the number of starting changing-points. In our analysis, almost all the detected change-points were identified as single change-points. Note that we also imposed some manual constraints on the paired change-points to avoid the overlaps of two neighbouring pairs and discard some single change-points with obvious deviations. For example, the first detected change-point in the station 031124 was identified as an ending change-point at the second day of the analyzed period, while we expected the starting change-point to be $3 - 7$ days preceding the detected ending change-point, so that we discarded this change-point.

5.1.2 Hypothesis test

As discussed in Section 3, the overall trend of GPS data is a noisy linear process if no SSE occurs, while the occurrence of an SSE redirects the original trend in a different direction. Upon completion of the SSE, the trend reverses back to its previous state. As shown in Fig. 2, the sign of the displacement rate at the start time of an SSE is opposite to that of the secular displacement rate. The sign change of the displacement rate at the start times of SSEs constitutes the basis of the null hypothesis test, therefore the following tests are only conducted on the starting change-points. In our tests, the null hypothesis is that SSEs do not occur, and the alternative hypothesis is that SSEs occur. Following the approach of Yano and Kano (2022), the test statistic for testing if the k-th starting change-point at the j-th station is associated with an SSE can be set as

$$\bar{B}_j^k = \operatorname{sgn}\left(v_0^j\right) B_j^k = \operatorname{sgn}\left(v_0^j\right) \frac{\bar{v}_k^j - \bar{v}_0^j}{\frac{1}{\bar{N}_s^j - 1}\sqrt{\sum_{k=1}^{\bar{N}_s^j} (\bar{v}_k^j - \bar{v}_0^j)^2}}, \tag{6}$$

where sgn refers to the sign function; and $\bar{v}_k^j$ and $\bar{v}_0^j$ refer to the displacement rate at the k-th starting change-point and the secular displacement rate of the j-th station, respectively. We estimate the probability that SSEs do not occur at the k-th starting point of the j-th station by

$$p_j^k = \mathbb{P}\left(B \leq \bar{B}_j^k\right) = \bar{\Phi}\left(\bar{B}_j^k\right), \tag{7}$$

where $\bar{\Phi}(\cdot)$ refers to the cumulative distribution function of the standard Gaussian distribution. The closer $\bar{\Phi}\left(\bar{B}_j^k\right)$ is to 0, the more confidently we can reject the null hypothesis. To reduce Type I errors, we combine p-values of stations neighbouring the j-th station into a new single p-value through the harmonic mean p-value method (Wilson, 2019; Yano & Kano, 2022), denoted by $\hat{p}_j^k$. Finally, we quantify the confidence of occurrence of SSEs by

$$\tilde{p}_j^k = 1 - \hat{p}_j^k. \tag{8}$$

More details about how to calculate $\tilde{p}_j^k$ can be found in the supplement and in Yano and Kano (2022).

5.1.3 Identifying SSE candidates

Fig. 9 presents the estimated probability of each detected change-point for the occurrence of an SSE by the null hypothesis test and its associated SSE category. We observe that at most stations SSAID can successfully detect SSEs with high confidence. At several stations, no such change-points are found, such as stations 021052 and 950449. The best detection happened at station 950447, in which all the four detected change-points have high confidence value of $\tilde{p}_j^k \geq 0.9$.

Based on the estimated $\tilde{p}_j^k$ values, we categorize the detected change-points into probable, possible and non-SSE SSE candidates, if $\tilde{p}_j^k \geq 0.9$ and $\hat{N}_a^j > 1$; $0.6 \leq \tilde{p}_j^k < 0.9$ or $\tilde{p}_j^k \geq 0.9$ with $\hat{N}_a^j = 1$; and $\tilde{p}_j^k < 0.6$, respectively. The introduction of $\hat{N}_a^j > 1$ in the definition of probable SSE candidates is to guarantee that the detected change-points have a high confidence for the occurrence of SSEs at neighbouring stations within 30 km simultaneously, rather than at a single station (Yano & Kano, 2022). Under the current classification rules, we only have a high confidence that detected change-points in the first group are associated with SSEs, and we are less confident that the other detected change-points are associated with SSEs. Fig. 9 (b) indicates that we have identified 39 probable SSE candidates (see green circles) and 31 possible SSE candidates (see

light green triangles) in total across all the stations. Note that some detected SSEs at different stations might be from the same SSE, indicating that the actual number of detected SSEs is likely less than the number stated above (see details in the subsequent discussions). In addition, detected change-points classified as non-SSEs still might be associated with SSEs, as other unknown non-tectonic movements or noise could affect the displacement field at the observation site so that the sign change does not significantly differ from the secular displacement rate (Nishimura et al., 2013). In the remainder of this study, we do not discuss these 2 groups further and instead we focus on the detected change-points in the first group of probable SSE candidates.

5.1.4 Comparison and validation

During the period analyzed in our current study, 8 SSEs were identified in the western Shikoku region along the Bungo Channel by Nishimura et al. (2013) (see orange shaded-areas in Fig. 10 (a); the associated SSE catalogue obtained from Kano et al., 2018). Not only has our new method successfully detected all these 8 SSEs in various stations, but SSAID is also able to detect many more previously undetected probable SSE candidates. Note that it is not expected that all the SSEs can be recorded at each GPS station, since the SNR and ground displacements caused by SSEs might greatly vary at different stations. If the SNR is too low or the ground displacement is too small at a certain station, the change-points associated with SSEs cannot be detected.

To further verify the validity of the newly detected probable SSEs, we investigate their correlations with the tremor occurrence, since tremors often accompany SSEs (Rogers & Dragert, 2003; Obara & Kato, 2016; Wang et al., 2018). An increasing daily number of tremors generally indicates that an SSE is probably occurring (Ito et al., 2007). Note that the occurrence of SSEs is not always consistent with tremor activity, which means that SSEs can also occur when no tremor activity is detected (Wang et al., 2018; Kano & Kato, 2020; Yano & Kano, 2022). In addition, not all the observed tremors are associated with the occurrence of SSEs. Based on their recurrence pattern, the tremors in the Shikoku region have been categorized into three states: episodic; weak concentration and background by Wang et al. (2018), among which only the tremors in the episodic state occur during SSEs. Therefore, we count the number of daily tremors in the episodic state to investigate its correlation with SSEs. As the 36 GPS stations used in our study are concentrated in the western Shikoku region (see Fig. 1 (b)), we only utilize the episodic tremors around these GPS stations (i.e. with state index 1-7 and 9-13 as indicated in Wang et al., 2018), rather than the whole observed tremor catalogue in the Shikoku region. Fig. 10 (a) and (b) show that the identified probable SSEs are well concordant with tremor activity in the episodic states. We also notice that at its highest peaks, the number of tremors is about 20, much less than that of the identified probable SSEs (i.e. 39) during the study period. This is sensible, because the same SSE might be recorded simultaneously by different GPS stations, as expected.

5.2 Fault estimation

Potential SSEs are expected to bring up a systematic pattern change in the displacement field at various stations, however the above hypothesis tests fail to consider such changes in the displacement field (Nishimura et al., 2013). This can be done by estimating a fault model to describe the observed displacements (Nishimura et al., 2013; Nishimura, 2021; Yano & Kano, 2022). We use a Bayesian inversion method, i.e. the Markov chain Monte Carlo (MCMC) method with the Metropolis-Hastings algorithm (Bagnardi & Hooper, 2018; Yano & Kano, 2022), to estimate a finite rectangular fault model with uniform slip for each detected probable SSE, and systematically investigate its associated displacement field. This rectangular fault model is the same as that used in Okada (1985). Based on the processed cumulative displacement field as shown in Eq. (3), the displacement field for each probable SSE candidate at various GPS stations can be sim-

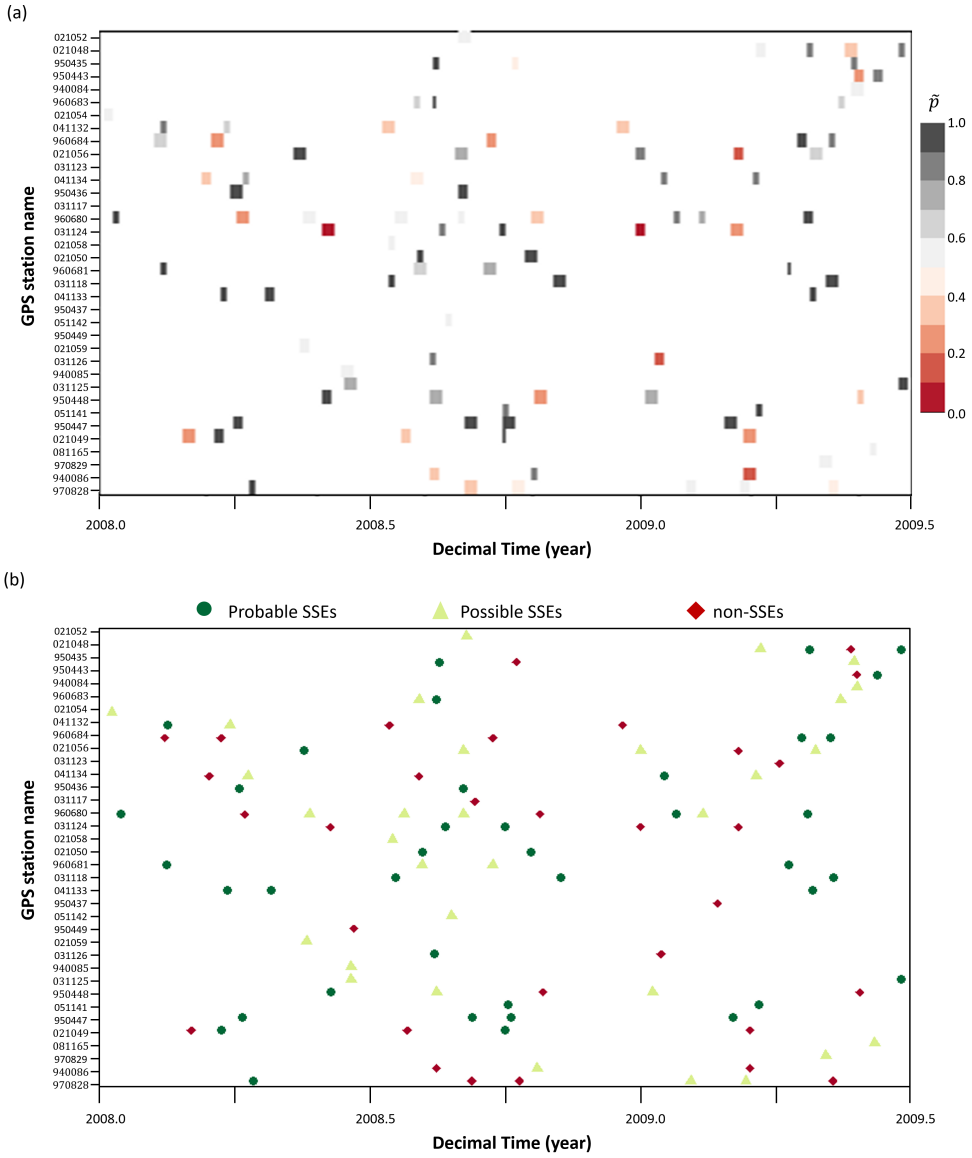

Figure 9. (a) Estimated confidence $\tilde{p}$ of each change-point pair shown in Fig. 7 (b). The left and the right side of each rectangle refer to the starting and the ending change-point, respectively. The width of each rectangular along the time axis denotes the duration of the associated potential SSE. (b) Detected SSEs categorised as probable SSEs (green circles), possible SSEs (light green triangles) and non-SSEs (red diamonds). The location of each marker refers to the middle time of each SSE candidate.

ply quantified by subtracting the cumulative displacement field at the starting change-point from that at the ending change-point. These estimated daily displacement variations are used to obtain the fault estimation.

We formulate the observed displacement field at a single station as

$$\mathbf{d} = \mathbf{G}(\mathbf{m}) + \boldsymbol{\epsilon}, \tag{9}$$

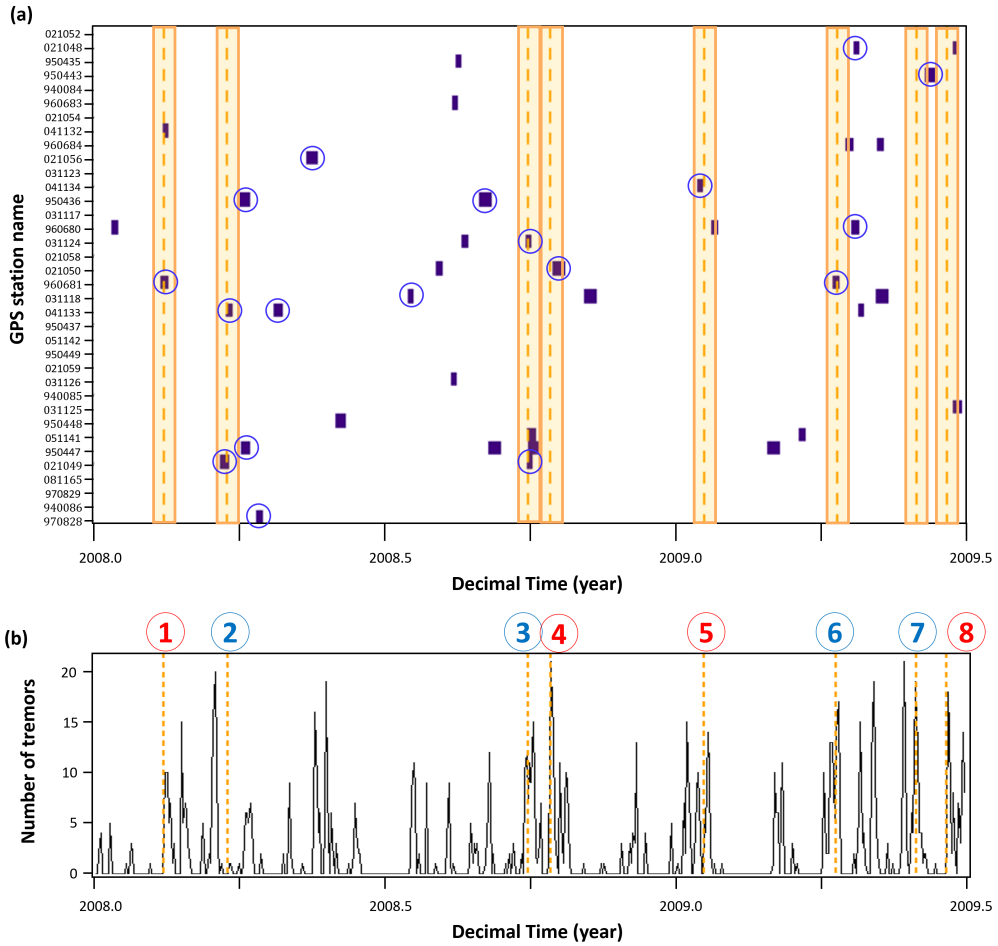

Figure 10. (a) The distribution of detected probable SSEs by SSAID, which are indicated by purple boxes. The left and the right sides of each purple box refer to the start and end times of an identified probable SSE by null hypothesis tests, respectively. Orange dotted lines in the middle of each shaded area refer to the occurrence times of SSEs identified by Nishimura et al. (2013). We assume that the start and end times of their identified SSEs are 7 days before and after the occurrence times, respectively. Purple boxes highlighted by blue circles refer to probable SSEs identified by the fault estimation (see Section 5.2). (b) The daily number of tremors in the episodic state. Numbers in circles on the top refer to the index of identified SSEs by Nishimura et al. (2013) in Shikoku region. SSEs indicated by blue numbers are located within our research area, while those indicated by red numbers are located in the eastern Shikoku region.

where $\mathbf{d} = (d_e, d_n, d_z)$ is the data vector containing the displacement components along different directions (i.e. east, north and vertical); $\mathbf{m} = (m_1, \cdots, m_9)$ contains the 9 fault model parameters to be estimated including length, width, depth, latitude, longitude, strike, rake, slip and dip angle; $\mathbf{G}$ describes the forward nonlinear model that calculates the synthetic displacements (see Okada, 1985); and $\boldsymbol{\epsilon}$ describes the error along different directions.

Under the Bayesian framework, the posterior probability density function to quantify how well the source model $\mathbf{m}$ describes the observed data $\mathbf{d}$ can be calculated by

$$\mathbb{P}\left(\mathbf{m}|\mathbf{d}\right) = \frac{\mathbb{P}\left(\mathbf{d}|\mathbf{m}\right)\mathbb{P}\left(\mathbf{m}\right)}{\mathbb{P}\left(\mathbf{d}\right)}, \tag{10}$$

where $\mathbb{P}\left(\mathbf{d}|\mathbf{m}\right)$ is the likelihood function to calculate the probability of obtaining the observed data $\mathbf{d}$ given the source model $\mathbf{m}$; $\mathbb{P}\left(\mathbf{m}\right)$ is the prior information on the probability density function of the source model; and $\mathbb{P}\left(\mathbf{d}\right)$ is a normalizing constant, which is independent of the source model (Amey et al., 2018; Bagnardi & Hooper, 2018). For GPS data, although prior information on $\mathbb{P}\left(\mathbf{m}\right)$ is generally not available, it can be estimated by the uninformative Jeffreys prior (Ulrych et al., 2001; Bagnardi & Hooper, 2018). Assuming that the errors in the observed data vector obey the Gaussian distribution with a mean of zero and covariance matrix $\mathbf{C}_e$, i.e. $\boldsymbol{\epsilon} \sim (\mathbf{0}, \mathbf{C}_e)$, the likelihood function is then estimated by

$$\mathbb{P}\left(\mathbf{d}|\mathbf{m}\right) = (2\pi)^{-\mathring{N}/2}|\mathbf{C_e}|^{-1/2}\exp\left(-\frac{1}{2}\mathbf{r}^T\mathbf{C_e}^{-1}\mathbf{r}\right), \tag{11}$$

where $\mathring{N}$ is the total number of data observations, the notation $|\cdot|$ and the superscript T refer to the determinant and the transpose of a matrix, respectively, the superscript -1 denotes matrix inversion, and $\mathbf{r} = \mathbf{d} - \mathbf{G}\left(\mathbf{m}\right)$ is the residual between the synthetic data and the observed data. When inverting GPS data, the data vector $\mathbf{d}$ is formed from multiple data recorded by different stations, i.e. $\mathbf{d} = \{d_h^j | j = 1, \cdots, \hat{N}_c; h = e, n, z\}$, where $\hat{N}_c$ is the number of stations used for the current inversion; j and h are the station index and the component index, respectively. For multiple data sets, assuming that they are independent from each other, the associated likelihood function is then calculated by

$$\mathbb{P}\left(\mathbf{d}|\mathbf{m}\right) = \Pi_{j=1}^{\hat{N}_c}(2\pi)^{-\mathring{N}_j/2}|\mathbf{C_e^{(j)}}|^{-1/2}\exp\left(-\frac{1}{2}\mathbf{r_j}^T\mathbf{C_e^{(j)}}^{-1}\mathbf{r_j}\right), \tag{12}$$

where $\mathring{N}_j$ is the total number of data observations at the j-th station, and $\mathbf{C_e^{(j)}}$ and $\mathbf{r_j}$ are the covariance matrix and the residual of the data set recorded by the j-th station, respectively. Given an initial model $\mathbf{m_0}$, the MCMC method will iteratively explore the space of model parameters through an automatic step selection until the maximum number of iterations is reached, and a set of source parameters with the maximum a posteriori probability solution is then extracted as the optimal model to best characterize the observed data (Bagnardi & Hooper, 2018).

For each identified probable SSE (see purple boxes in Fig. 10 (a)), we only use the observed displacement data of neighbouring stations within a designated range as the input data of the inversion. Here, the ranges that we utilize along the dip and the strike directions are 100 km and 150 km, respectively, from the station where the probable SSE was identified (Takagi et al., 2019). We further rule out the data with a high percentage of invalid values (i.e. $\geq 20\%$) during the period analyzed in our study (Nishimura, 2021). Our inversion approach is divided into two stages. First, we take the approach of Yano and Kano (2022) to fully explore the source parameters while we further assume that no tensile component occurs, thus nine source parameters need to be determined, i.e. length, width, strike, dip, depth, slip, rake, latitude, longitude. The initial guesses for those nine source parameters are set as follows: the latitude and the longitude of the estimated fault are set as those of the station where the probable SSE candidate was identified; the length and the width are 50 km and 35 km, respectively; the slip amount and the rake angle are 10 mm and 110°, respectively; the initial values for the strike, the dip and the depth are obtained by projecting the estimated fault model to the surface of the Philippine Sea Plate. To mitigate the effect of the initial model on the final inversion results, we further simulate 9 realisations of the initial fault model obtained by randomly perturbing the default model described above. In total, we run the MCMC inversion 10

times for each detected probable SSE. We then choose the output of these 10 sets with the smallest residual as a new set of initial model parameters, and conduct a new inversion (Bagnardi & Hooper, 2018; Nishimura, 2021).

In the second stage, we take the output fault models from the first stage as a new initial model, but we now follow the approach of Nishimura et al. (2013), which assumes that the depth, strike and dip angle of the fault model are dependent on its location to fit the surface of the Philippine Sea Plate. This means that we have 6 free parameters instead of the previous 9 free parameters. We then estimate a final finite fault model for each probable SSE candidate. As the slip direction of the expected SSEs in the Shikoku region should be opposite to the plate convergence direction (i.e. N50°W), we rule out probable SSEs candidates, for which slip directions are not between N100°E and N170°E (Nishimura et al., 2013).

We obtain 18 potential SSEs in our current research area (see blue circles in Fig. 10 (a)). Fig. 11 shows representative examples of estimated fault models for four identified probable SSEs (see the other results in the supplement). These identified SSEs have an opposite slip direction to that of the plate convergence. The locations of some estimated faults coincide well with the epicenters of the tremors (see Fig. 11 (a) and (b)), suggesting the possible occurrence of episodic tremor and slip (ETS). We also notice that no tremor activities were observed around the estimated fault model in Fig. 11 (c) and (d), even though the estimated location is still close to the locations of known SSEs (see Fig. 1 (a)).

6 Conclusions

We developed a novel statistical method to automatically detect short-term SSEs in GPS data. We demonstrated its effectiveness on a range of noisy simulated SSE data and illustrated its superior detection performance compared to two existing detection methods, i.e. linear regression with ΔAIC and l_1 trend filtering. We then applied SSAID to detect short-term SSEs in observed GPS data in the western Shikoku region. The results show that SSAID successfully detects multiple change-points in various GPS stations. We utilized the null hypothesis test to identify probable SSE candidates from these detected change-points, based on the sign of the displacement rate being different from that of the secular displacement rate. These SSE candidates include all known SSEs identified by Nishimura et al. (2013) during the period analyzed, as well as previously undetected SSEs. We further estimated the parameters of a finite fault model generating the observed displacement field for each probable SSE candidate using a Bayesian inversion technique. Selecting the SSEs for which the azimuth directions of the slip vectors of the estimated fault models are opposite to that of the plate convergence, we managed to identify new SSEs in the western Shikoku region that should be added to the existing catalogue. Our results demonstrate the effectiveness of SSAID in detecting SSEs in observed GPS data.

7 Open Research

Data and Code Availability Statement The simulated SSE data used for numerical tests in the study and the code of the newly developed method SSAID are available at Github via `https://github.com/yiming-otago/SSAID`, which are provided for private study and research purposes and are protected by copyright with all rights reserved unless otherwise indicated. The observed GPS data utilized in this study can be requested through Geospatial Information Authority of Japan (GSI) at `https://www.gsi.go.jp/ENGLISH/geonet_english.html`.

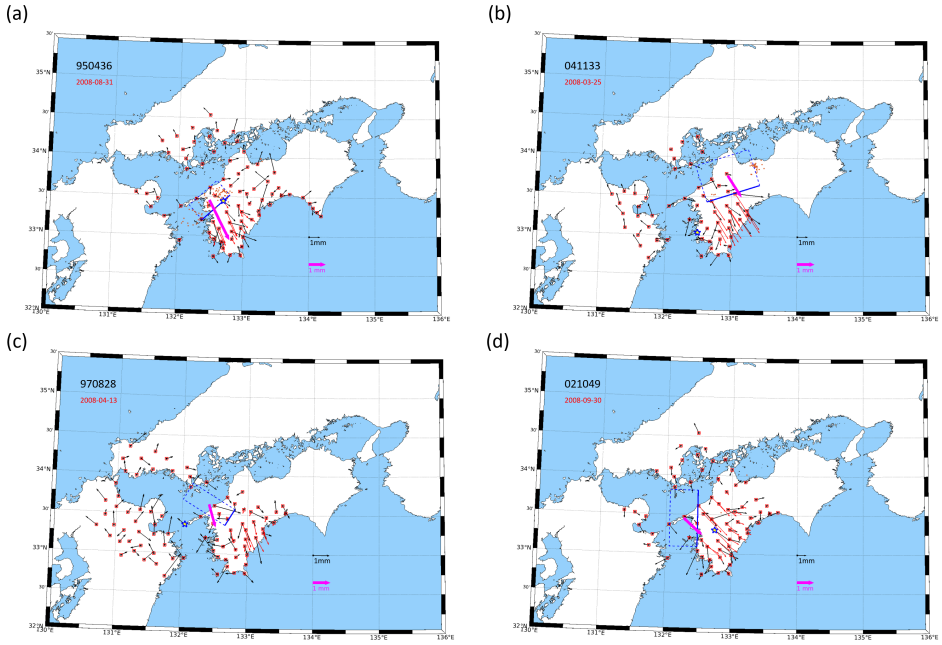

Figure 11. Representative examples of the estimated fault model for identified probable SSE candidates at the different stations: (a) station 970828; (b) station 021049; (c) station 950436; (d) station 041133. The date in red under the site name refers to the start date of this probable SSE candidate. The star in the map indicates the location of the station where this SSE candidate was identified. The black and the pink arrows in the right-bottom corner are the scale arrows for the observed displacement and the slip amount of the estimated model, respectively. The synthetic displacements by the displacement model of Okada (1985) have the same arrow scale as the observed ones. Orange dots indicate the epicentre of tremors in the episodic state 5 days before and after the date (see the date on the left-upper corner) when this candidate was found. The blue solid line of the rectangle refers to the top edge of the estimated fault model.

Acknowledgments

We are grateful to Associate Professor Ting Wang (University of Otago) for her constant support, insightful discussions, and technical assistance throughout this project. Her expertise and guidance played a crucial role in shaping the direction of this research. We would also like to thank Assistant Professor Akiko Takeo (University of Tokyo) and Associate Professor Takuya Nishimura (Kyoto University) for kindly sharing the processed GPS data and the geometry file of the Philippine Sea Plate surface with us. We further acknowledge the helpful comments and suggestions from Associate Professor Takuya Nishimura on the current work. Y.M. was supported by a University of Otago Doctoral Scholarship, and University of Otago Postgraduate Publishing Bursaries (Doctoral).

References

Amey, R., Hooper, A., & Walters, R. (2018). A bayesian method for incorporating self-similarity into earthquake slip inversions. *Journal of Geophysical Research: Solid Earth*, *123*(7), 6052–6071.

Anastasiou, A., & Fryzlewicz, P. (2021). Detecting multiple generalized change-points by isolating single ones. *Metrika*, 1–34.

Bagnardi, M., & Hooper, A. (2018). Inversion of surface deformation data for rapid estimates of source parameters and uncertainties: A bayesian approach. *Geochemistry, Geophysics, Geosystems*, *19*(7), 2194–2211.

Barbot, S. (2019). Slow-slip, slow earthquakes, period-two cycles, full and partial ruptures, and deterministic chaos in a single asperity fault. *Tectonophysics*, *768*, 228171.

Bartlow, N. M., Wallace, L. M., Beavan, R. J., Bannister, S., & Segall, P. (2014). Time-dependent modeling of slow slip events and associated seismicity and tremor at the hikurangi subduction zone, new zealand. *Journal of Geophysical Research: Solid Earth*, *119*(1), 734–753.

Bedford, J., & Bevis, M. (2018). Greedy automatic signal decomposition and its application to daily gps time series. *Journal of Geophysical Research: Solid Earth*, *123*(8), 6992–7003.

Beeler, N. M., Roeloffs, E., & McCausland, W. (2014). Re-estimated effects of deep episodic slip on the occurrence and probability of great earthquakes in cascadia. *Bulletin of the Seismological Society of America*, *104*(1), 128–144.

Bletery, Q., & Nocquet, J.-M. (2020). Slip bursts during coalescence of slow slip events in cascadia. *Nature communications*, *11*(1), 1–6.

Cavalié, O., Pathier, E., Radiguet, M., Vergnolle, M., Cotte, N., Walpersdorf, A., ... Cotton, F. (2013). Slow slip event in the mexican subduction zone: Evidence of shallower slip in the guerrero seismic gap for the 2006 event revealed by the joint inversion of insar and gps data. *Earth and Planetary Science Letters*, *367*, 52–60.

Chen, Q., van Dam, T., Sneeuw, N., Collilieux, X., Weigelt, M., & Rebischung, P. (2013). Singular spectrum analysis for modeling seasonal signals from gps time series. *Journal of Geodynamics*, *72*, 25–35.

Crowell, B. W., Bock, Y., & Liu, Z. (2016). Single-station automated detection of transient deformation in gps time series with the relative strength index: A case study of cascadian slow slip. *Journal of Geophysical Research: Solid Earth*, *121*(12), 9077–9094.

Davis, J. L., Wernicke, B. P., & Tamisiea, M. E. (2012). On seasonal signals in geodetic time series. *Journal of Geophysical Research: Solid Earth*, *117*(B1).

Dong, D., Fang, P., Bock, Y., Webb, F., Prawirodirdjo, L., Kedar, S., & Jamason, P. (2006). Spatiotemporal filtering using principal component analysis and karhunen-loeve expansion approaches for regional gps network analysis. *Journal of geophysical research: solid earth*, *111*(B3).

ElGharbawi, T., & Tamura, M. (2015). Coseismic and postseismic deformation estimation of the 2011 tohoku earthquake in kanto region, japan, using insar time series analysis and gps. *Remote Sensing of Environment*, *168*, 374–387.

Fujita, M., Nishimura, T., & Miyazaki, S. (2019). Detection of small crustal deformation caused by slow slip events in southwest japan using gnss and tremor data. *Earth, Planets and Space*, *71*(1), 1–13.

Fukuda, J., Higuchi, T., Miyazaki, S., & Kato, T. (2004). A new approach to time-dependent inversion of geodetic data using a monte carlo mixture kalman filter. *Geophysical Journal International*, *159*(1), 17–39.

Fukuda, J., Miyazaki, S., Higuchi, T., & Kato, T. (2008). Geodetic inversion for space—time distribution of fault slip with time-varying smoothing regularization. *Geophysical Journal International*, *173*(1), 25–48.

Ghil, M., Allen, M., Dettinger, M., Ide, K., Kondrashov, D., Mann, M., ... others (2002). Advanced spectral methods for climatic time series. *Reviews of geophysics*, *40*(1), 3–1.

Granat, R., Parker, J., Kedar, S., Dong, D., Tang, B., & Bock, Y. (2013). Statistical approaches to detecting transient signals in gps: Results from the 2009–2011 transient detection exercise. *Seismological Research Letters*, *84*(3), 444–454.

Haines, J., Wallace, L. M., & Dimitrova, L. (2019). Slow slip event detection in cascadia using vertical derivatives of horizontal stress rates. *Journal of Geophysical Research: Solid Earth*, *124*(5), 5153–5173.

He, X., Montillet, J.-P., Fernandes, R., Bos, M., Yu, K., Hua, X., & Jiang, W. (2017). Review of current gps methodologies for producing accurate time series and their error sources. *Journal of Geodynamics*, *106*, 12–29.

Hirose, H., Hirahara, K., Kimata, F., Fujii, N., & Miyazaki, S. (1999). A slow thrust slip event following the two 1996 hyuganada earthquakes beneath the bungo channel, southwest japan. *Geophysical Research Letters*, *26*(21), 3237–3240.

Hirose, H., Kimura, H., Enescu, B., & Aoi, S. (2012). Recurrent slow slip event likely hastened by the 2011 tohoku earthquake. *Proceedings of the National Academy of Sciences*, *109*(38), 15157–15161.

Hirose, H., & Kimura, T. (2020). Slip distributions of short-term slow slip events in shikoku, southwest japan, from 2001 to 2019 based on tilt change measurements. *Journal of Geophysical Research: Solid Earth*, *125*(6), e2020JB019601.

Hirose, H., & Obara, K. (2010). Recurrence behavior of short-term slow slip and correlated nonvolcanic tremor episodes in western shikoku, southwest japan. *Journal of Geophysical Research: Solid Earth*, *115*(B6).

Ikari, M. J., Marone, C., Saffer, D. M., & Kopf, A. J. (2013). Slip weakening as a mechanism for slow earthquakes. *Nature geoscience*, *6*(6), 468–472.

Ito, Y., Hino, R., Kido, M., Fujimoto, H., Osada, Y., Inazu, D., ... others (2013). Episodic slow slip events in the japan subduction zone before the 2011 tohoku-oki earthquake. *Tectonophysics*, *600*, 14–26.

Ito, Y., Obara, K., Shiomi, K., Sekine, S., & Hirose, H. (2007). Slow earthquakes coincident with episodic tremors and slow slip events. *Science*, *315*(5811), 503–506.

Ji, K. H., & Herring, T. A. (2013). A method for detecting transient signals in gps position time-series: smoothing and principal component analysis. *Geophysical Journal International*, *193*(1), 171–186.

Jiang, Y., Wdowinski, S., Dixon, T. H., Hackl, M., Protti, M., & Gonzalez, V. (2012). Slow slip events in costa rica detected by continuous gps observations, 2002–2011. *Geochemistry, Geophysics, Geosystems*, *13*(4).

Jordan, T. H., & Jones, L. M. (2010). Operational earthquake forecasting: Some thoughts on why and how. *Seismological Research Letters*, *81*(4), 571–574.

Kano, M., Aso, N., Matsuzawa, T., Ide, S., Annoura, S., Arai, R., ... others (2018). Development of a slow earthquake database. *Seismological Research Letters*, *89*(4), 1566–1575.

Kano, M., & Kato, A. (2020). Detailed spatial slip distribution for short-term slow slip events along the nankai subduction zone, southwest japan. *Journal of Geophysical Research: Solid Earth*, *125*(7), e2020JB019613.

Lohman, R. B., & Murray, J. R. (2013). The scec geodetic transient detection validation exercise. *Seismological Research Letters*, *84*(3), 419–425.

Ma, Y. (2022). *Mathematical and statistical modelling of slow slip events* (Unpublished doctoral dissertation). University of Otago.

Ma, Y., Anastasiou, A., Wang, T., & Montiel, F. (2022). Detecting change-points in noisy gps time series with continuous piecewise structures. *arXiv preprint arXiv:2202.12414*.

Mazzotti, S., & Adams, J. (2004). Variability of near-term probability for the next great earthquake on the cascadia subduction zone. *Bulletin of the Seismologi-*

cal Society of America, *94*(5), 1954–1959.

McCaffrey, R. (2009). Time-dependent inversion of three-component continuous gps for steady and transient sources in northern cascadia. *Geophysical Research Letters*, *36*(7).

McGuire, J. J., & Segall, P. (2003). Imaging of aseismic fault slip transients recorded by dense geodetic networks. *Geophysical Journal International*, *155*(3), 778–788.

Melbourne, T. I., Szeliga, W. M., Miller, M. M., & Santillan, V. M. (2005). Extent and duration of the 2003 cascadia slow earthquake. *Geophysical Research Letters*, *32*(4).

Mitsui, N., & Hirahara, K. (2006). Slow slip events controlled by the slab dip and its lateral change along a trench. *Earth and Planetary Science Letters*, *245*(1-2), 344–358.

Miyazaki, S., & Heki, K. (2001). Crustal velocity field of southwest japan: Subduction and arc-arc collision. *Journal of Geophysical Research: Solid Earth*, *106*(B3), 4305–4326.

Miyazaki, S., McGuire, J. J., & Segall, P. (2003). A transient subduction zone slip episode in southwest japan observed by the nationwide gps array. *Journal of Geophysical Research: Solid Earth*, *108*(B2).

Nikolaidis, R. (2002). *Observation of geodetic and seismic deformation with the global positioning system*. University of California, San Diego.

Nishikawa, T., Matsuzawa, T., Ohta, K., Uchida, N., Nishimura, T., & Ide, S. (2019). The slow earthquake spectrum in the japan trench illuminated by the s-net seafloor observatories. *Science*, *365*(6455), 808–813.

Nishimura, T. (2014). Short-term slow slip events along the ryukyu trench, southwestern japan, observed by continuous gnss. *Progress in Earth and Planetary Science*, *1*(1), 1–13.

Nishimura, T. (2021). Slow slip events in the kanto and tokai regions of central japan detected using global navigation satellite system data during 1994–2020. *Geochemistry, Geophysics, Geosystems*, *22*(2), e2020GC009329.

Nishimura, T., Matsuzawa, T., & Obara, K. (2013). Detection of short-term slow slip events along the nankai trough, southwest japan, using gnss data. *Journal of Geophysical Research: Solid Earth*, *118*(6), 3112–3125.

Obara, K. (2020). Characteristic activities of slow earthquakes in japan. *Proceedings of the Japan Academy, Series B*, *96*(7), 297–315.

Obara, K., & Kato, A. (2016). Connecting slow earthquakes to huge earthquakes. *Science*, *353*(6296), 253–257.

Ohtani, R., McGuire, J. J., & Segall, P. (2010). Network strain filter: A new tool for monitoring and detecting transient deformation signals in gps arrays. *Journal of Geophysical Research: Solid Earth*, *115*(B12).

Okada, Y. (1985). Surface deformation due to shear and tensile faults in a half-space. *Bulletin of the Seismological Society of America*, *75*(4), 1135–1154.

Okada, Y., Nishimura, T., Tabei, T., Matsushima, T., & Hirose, H. (2022). Development of a detection method for short-term slow slip events using gnss data and its application to the nankai subduction zone. *Earth, Planets and Space*, *74*(1), 1–18.

Ozawa, S. W., Hatano, T., & Kame, N. (2019). Longer migration and spontaneous decay of aseismic slip pulse caused by fault roughness. *Geophysical Research Letters*, *46*(2), 636–643.

Radiguet, M., Perfettini, H., Cotte, N., Gualandi, A., Valette, B., Kostoglodov, V., ... Campillo, M. (2016). Triggering of the 2014 mw7. 3 papanoa earthquake by a slow slip event in guerrero, mexico. *Nature Geoscience*, *9*(11), 829–833.

Riel, B., Simons, M., Agram, P., & Zhan, Z. (2014). Detecting transient signals in geodetic time series using sparse estimation techniques. *Journal of Geophysical Research: Solid Earth*, *119*(6), 5140–5160.

Rogers, G., & Dragert, H. (2003). Episodic tremor and slip on the cascadia subduction zone: The chatter of silent slip. *Science*, *300*(5627), 1942–1943.

Rousset, B., Campillo, M., Lasserre, C., Frank, W. B., Cotte, N., Walpersdorf, A., ... Kostoglodov, V. (2017). A geodetic matched filter search for slow slip with application to the mexico subduction zone. *Journal of Geophysical Research: Solid Earth*, *122*(12), 10–498.

Saffer, D. M., & Wallace, L. M. (2015). The frictional, hydrologic, metamorphic and thermal habitat of shallow slow earthquakes. *Nature Geoscience*, *8*(8), 594–600.

Segall, P., Bürgmann, R., & Matthews, M. (2000). Time-dependent triggered afterslip following the 1989 loma prieta earthquake. *Journal of Geophysical Research: Solid Earth*, *105*(B3), 5615–5634.

Segall, P., Desmarais, E. K., Shelly, D., Miklius, A., & Cervelli, P. (2006). Earthquakes triggered by silent slip events on kīlauea volcano, hawaii. *Nature*, *442*(7098), 71–74.

Segall, P., & Matthews, M. (1997). Time dependent inversion of geodetic data. *Journal of Geophysical Research: Solid Earth*, *102*(B10), 22391–22409.

Smith, E. F., & Gomberg, J. (2009). A search in strainmeter data for slow slip associated with triggered and ambient tremor near parkfield, california. *Journal of Geophysical Research: Solid Earth*, *114*(B12).

Takagi, R., Uchida, N., & Obara, K. (2019). Along-strike variation and migration of long-term slow slip events in the western nankai subduction zone, japan. *Journal of Geophysical Research: Solid Earth*, *124*(4), 3853–3880.

Ulrych, T. J., Sacchi, M. D., & Woodbury, A. (2001). A bayes tour of inversion: A tutorial. *Geophysics*, *66*(1), 55–69.

Vergnolle, M., Walpersdorf, A., Kostoglodov, V., Tregoning, P., Santiago, J., Cotte, N., & Franco, S. (2010). Slow slip events in mexico revised from the processing of 11 year gps observations. *Journal of Geophysical Research: Solid Earth*, *115*(B8).

Voss, N., Dixon, T. H., Liu, Z., Malservisi, R., Protti, M., & Schwartz, S. (2018). Do slow slip events trigger large and great megathrust earthquakes? *Science advances*, *4*(10), eaat8472.

Wallace, L. M. (2020). Slow slip events in new zealand. *Annual Review of Earth and Planetary Sciences*, *48*, 175–203.

Wallace, L. M., Hreinsdóttir, S., Ellis, S., Hamling, I., D'Anastasio, E., & Denys, P. (2018). Triggered slow slip and afterslip on the southern hikurangi subduction zone following the kaikōura earthquake. *Geophysical Research Letters*, *45*(10), 4710–4718.

Wallace, L. M., Kaneko, Y., Hreinsdóttir, S., Hamling, I., Peng, Z., Bartlow, N., ... Fry, B. (2017). Large-scale dynamic triggering of shallow slow slip enhanced by overlying sedimentary wedge. *Nature Geoscience*, *10*(10), 765–770.

Walwer, D., Calais, E., & Ghil, M. (2016). Data-adaptive detection of transient deformation in geodetic networks. *Journal of Geophysical Research: Solid Earth*, *121*(3), 2129–2152.

Wang, T., Zhuang, J., Buckby, J., Obara, K., & Tsuruoka, H. (2018). Identifying the recurrence patterns of nonvolcanic tremors using a 2-d hidden markov model with extra zeros. *Journal of Geophysical Research: Solid Earth*, *123*(8), 6802–6825.

Wdowinski, S., Bock, Y., Zhang, J., Fang, P., & Genrich, J. (1997). Southern california permanent gps geodetic array: Spatial filtering of daily positions for estimating coseismic and postseismic displacements induced by the 1992 landers earthquake. *Journal of Geophysical Research: Solid Earth*, *102*(B8), 18057–18070.

Williams, C. A., & Wallace, L. M. (2015). Effects of material property variations on slip estimates for subduction interface slow-slip events. *Geophysical Research*

Letters, *42*(4), 1113–1121.

Wilson, D. J. (2019). The harmonic mean p-value for combining dependent tests. *Proceedings of the National Academy of Sciences*, *116*(4), 1195–1200.

Yano, K., & Kano, M. (2022). l1 trend filtering-based detection of short-term slow slip events: Application to a gnss array in southwest japan. *Journal of Geophysical Research: Solid Earth*, *127*(5), e2021JB023258.

Yao, Y.-C. (1988). Estimating the number of change-points via schwarz'criterion. *Statistics & Probability Letters*, *6*(3), 181–189.

Yarai, H., & Ozawa, S. (2013). Quasi-periodic slow slip events in the afterslip area of the 1996 hyuga-nada earthquakes, japan. *Journal of Geophysical Research: Solid Earth*, *118*(5), 2512–2527.